The International Journal of Advanced Manufacturing Technology (2021) 115:2299–2312
https://doi.org/10.1007/s00170-021-07278-x

ORIGINAL ARTICLE

In situ investigation of nanometric cutting of 3C-SiC using scanning electron microscope

Dongyu Tian[1] · Zongwei Xu[1] · Lei Liu[1] · Zhanqi Zhou[1] · Junjie Zhang[2] · Xuesen Zhao[2] · Alexander Hartmaier[3] · Bing Liu[4] · Le Song[1] · Xichun Luo[5]

Received: 27 October 2020 / Accepted: 11 May 2021 / Published online: 22 May 2021

Abstract
Experimentally revealing the nanometric deformation behavior of 3C-SiC is challenging due to its ultra-small feature size for brittle-to-ductile transition. In the present work, we elucidated the nanometric cutting mechanisms of 3C-SiC by performing in situ nanometric cutting experiments under scanning electron microscope (SEM), as well as post-characterization by electron back-scattered diffraction (EBSD) and transmission electron microscopy (TEM). In particular, a new method based on the combination of image processing technology and SEM online observation was proposed to achieve in situ measurement of cutting force with an uncertainty less than 1 mN. Furthermore, the cutting cross-section was characterized by atomic force microscope (AFM) to access the specific cutting energy. The results revealed that the specific cutting energy increase non-linearly with the decrease of cutting depth due to the size effect of cutting tool in nanometric cutting. The high-pressure phase transformation (HPPT) may play the major role in 3C-SiC ductile machining under the parameters of this experiment.

Keywords Cubic silicon carbide · Diamond cutting · In situ SEM observation · Surface integrity · Phase transformation

1 Introduction

Silicon carbide (SiC) as a ceramic with outstanding mechanical and physical properties [1] has been recognized as a potential candidate material in future nuclear fusion reactors [2], petrochemical industries [3], large-scale quantum computing applications [4], laser devices [5], and space-based laser mirrors [6]. Among approximately 200 polytypes of SiC found at atmospheric pressure [7], 3C-SiC, as a cubic polytype (zinc blende structured) SiC, possesses the best stiffness to weight ratios, wear, and corrosion resistance [8]. Thus, 3C-SiC is suitable in the fabrication of semiconductor and optical devices for extreme environments. However, 3C-SiC exhibits poor machinability due to its hard and brittle characteristics [9].

The single point diamond turning (SPDT) has been proven as an efficient machining method for achieving ultra-smooth surfaces of brittle materials [10, 11]. SPDT enables brittle materials to be machined in ductile mode [12, 13]. Many researches were conducted to investigate the ductile deformation mechanisms of 3C-SiC such as pressure loading [14, 15], nanoindentation [16–18], nanoscratching [19, 20], and nanometric cutting [21, 22]. These studies have greatly increased the understanding of the ductile removal regime machining of cubic silicon carbide, but there still exist incongruence. For instance, Noreyan et al. [17] confirmed that the plastic behavior is related to the phase transition from the cubic zinc blende structure to the rocksalt structure under the indenter tip, which is in reasonable agreement with 3C-SiC pressure loading studies [14, 15]. While Szlufarska et al. [16] attributed the plastic behavior to dislocation nucleation and

✉ Zongwei Xu
zongweixu@tju.edu.cn

✉ Junjie Zhang
zhjj505@gmail.com

[1] State Key Laboratory of Precision Measuring Technology & Instruments, Tianjin University, Tianjin 300072, China

[2] Center for Precision Engineering, Harbin Institute of Technology, Harbin 150001, China

[3] Interdisciplinary Centre for Advanced Materials Simulation (ICAMS), Ruhr-University Bochum, 44780 Bochum, Germany

[4] School of Mechanical Engineering, Tianjin University of Commerce, Tianjin 300134, China

[5] Centre for Precision Manufacturing, Department of Design, Manufacture & Engineering Management, University of Strathclyde, Glasgow, UK

propagation without any high-pressure phase transformation. Whereas Zhao et al. [18] pointed out that shear slip is the predominant deformation mechanism in 3C-SiC during indentation. Tang [19] attributed the ductility of 3C-SiC to shear instability-induced amorphization. However, Goel et al. [21] claimed that the sp^3-sp^2 disorder transition causes the ductile response during the nanometric cutting process of 3C-SiC and 3C-SiC wears in a ductile manner by means of dislocation plasticity was considered by Szlufarska et al. [22].

However, the extant literature concerning nanometric cutting of SiC is seen to focus on simulation studies [21–31] and nanometric cutting experiments [32–34] are rarely reported due to its ultra-small feature size. It is of vital importance to carry out nanometric cutting experiments with high resolution characterization of 3C-SiC for the verification of simulation studies and the understanding of nanocutting mechanism of 3C-SiC.

Thus, cutting experiments were conducted by a nanometric cutting platform under high vacuum conditions in SEM/FIB dual beam system designed by Fang et al. [35] to provide accurate nanocutting motions with high resolution online observation. But due to the limit of the space and environment within the SEM vacuum chamber, the cutting force as an important parameter in revealing the interaction process of the cutting tools and the material cannot be detected in traditional ways. In this study, a new method for detecting cutting force by image processing technique was studied. Specific cutting energy was analyzed combined with the cutting cross-section information characterized by AFM. Then, EBSD and TEM were used to characterize possible phase transitions and dislocation movements in nanometric cutting. The EBSD and TEM results were further analyzed combined with cutting force and specific cutting energy results to investigate the material ductile removal mechanism of 3C-SiC in nanometric diamond cutting.

2 Experimental approaches

2.1 Experimental setup

In situ nanocutting experiments of single crystal 3C-SiC were conducted using a nanometric cutting stage integrated in SEM designed by Fang et al., as illustrated in Fig. 1a [35]. The nanocutting stage is placed directly below the SEM pole piece. Aiming at observing the material removal behavior more intuitively and obtain a flat machined surface in the nanometric cutting tests, a single crystal diamond cutting tool with a straight cutting edge length of 9 μm, as shown in Fig. 1b, was fabricated by focused ion beam (FIB) direct writing method [36] to perform the cutting experiments. The cutting experiments were conducted on the surface of 3C-SiC (100) with 99.90% EBSD pattern indexing rate as shown in Fig. 1c.

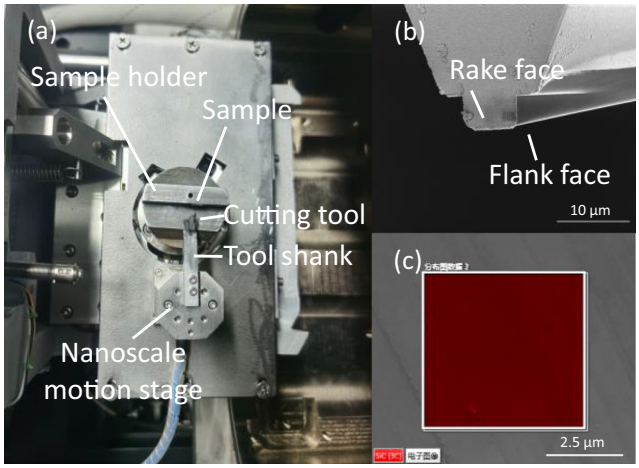

Fig. 1 Experimental setup. (**a**) Nanometric cutting stage integrated in SEM. (**b**) Morphology of the diamond cutting tool. (**c**) EBSD pattern of 3C-SiC sample

In order to obtain the online observation of the nanocutting process for the cutting force measurement, the cutting speed of approximately 117 nm/s was adopted.

2.2 Measurement of the cutting force

2.2.1 Principle of the cutting force measurement method

The cutting tool mounted on the tool shank via conductive silver glue was driven by a nanometric precision motion stage. The cutting tool moves horizontally during cutting process under SEM observation, which is shown in Fig. 2a. During the cutting process, the force condition of the cutting tool and tool shank can be deemed as a cantilever beam as illustrated in Fig. 2b. According to material mechanics, during nanometric cutting process, the cutting force (F) will cause deflection (y) at the force bearing point as shown in Fig. 2b. Therefore, this study proposes a new method of cutting force measurement, which combines the online observation function of SEM and image processing technology to detect the tiny nanometer deflection generated in nanometric cutting and then educe the cutting force. In this study, the SEM is applied to dynamic quantitative measurement of tiny physical quantities, which has not been applied in previous studies. The specific method steps were shown in Fig. 3.

The video of the tool idle running process and cutting process was recorded by SEM, and the trajectory of the cutting tool was extracted by image processing technique. The deflection information during cutting process was obtained by subtracting the idle running trajectory from the cutting process trajectory. Through the tool shank stiffness calibration experiment, the cutting force during nanometric cutting process under the corresponding deflection was educed to realize the measurement of the cutting force.

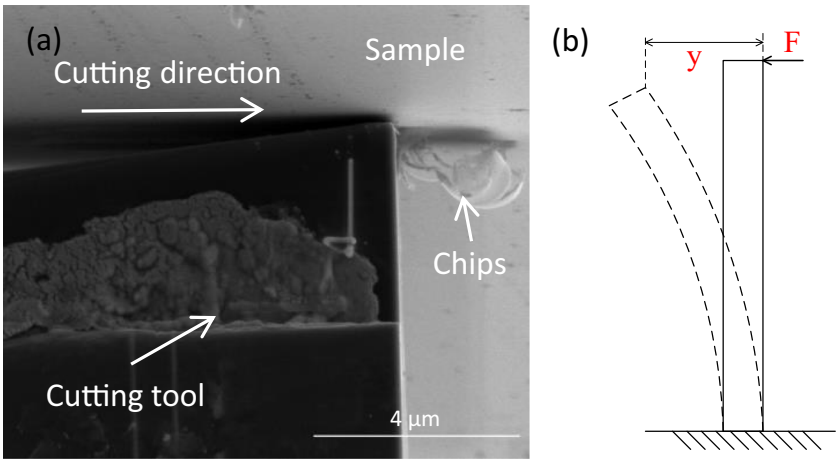

Fig. 2 (**a**) Nanocutting stage under SEM observation. (**b**) Sketch of simple two-dimensional cantilever beam

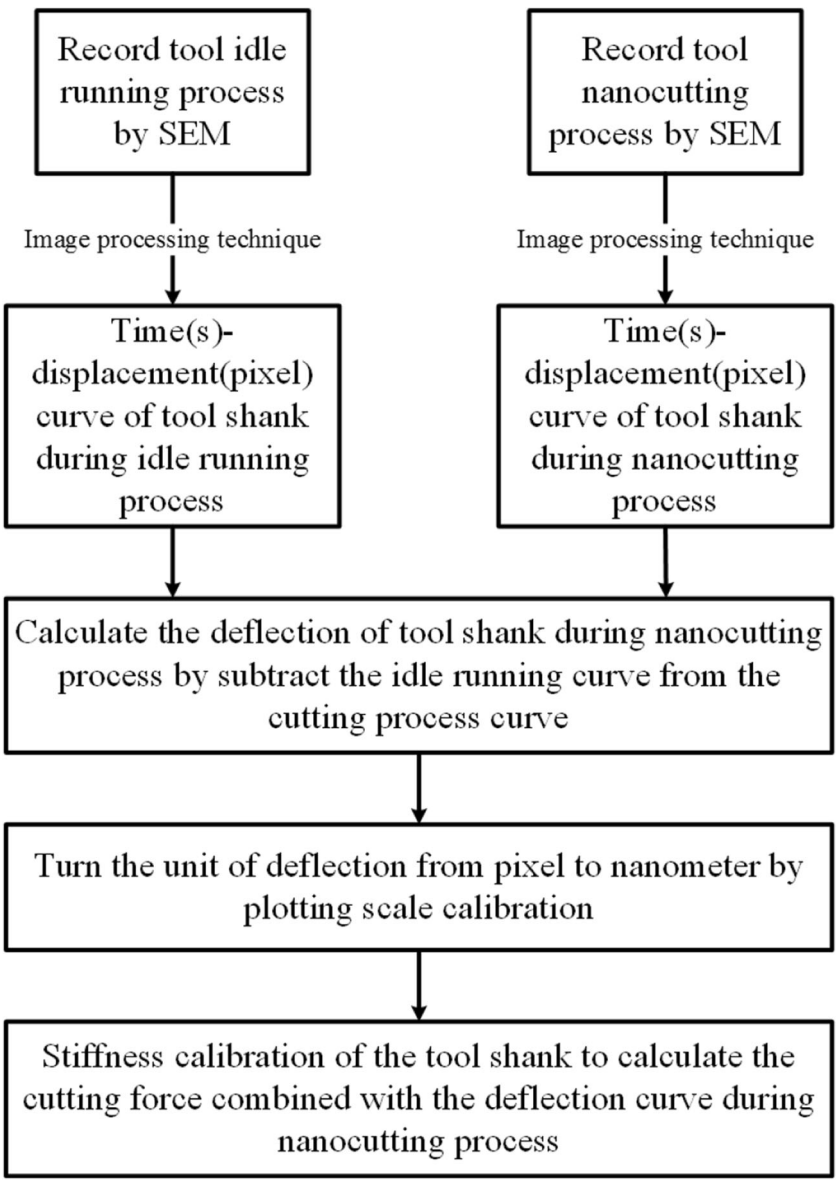

Fig. 3 Cutting force measurement by image processing technique

2.2.2 SEM imaging mechanism

In this study, image processing technology was used to process the video of the nanocutting process recorded by SEM to measure the cutting force. However, image processing technique is usually used for optical imaging systems. Applications in SEM imaging are rarely reported. The imaging mechanism of SEM is completely different from that of traditional optical systems. Therefore, the feasibility of image processing technology applied to SEM imaging needs to be studied. It is of great significance to investigate the SEM imaging mechanism and propose image processing technology methods suitable for SEM imaging. Figure 4 is the schematic illustration of SEM scanning trajectory. The electron beam is controlled to scan the sample in certain path to interact with samples and generate secondary electrons, which are received by the SEM detector to generate images. The time to scan an image is determined by the dwell time of electron beam and the image resolution. The dwell time and image resolution were chosen to be 100 ns and 1024×884 respectively to provide as much information of cutting process as possible while ensuring the signal-noise ratio (SNR). Under this condition, the frame time that SEM scan and generate an image is approximately 0.095 s. The frame rate of the video generated by the SEM recording function is 100 frames per second. Through frame-by-frame analysis of the SEM generated video, it is found that the image is updated approximately every 20 frames (0.20 s). The number of frames where the image was updated in the video recorded by SEM and the time interval were shown in Fig. 5. The update interval for most images is 0.20 s; this indicated that in the SEM generated video, the images of the video would be updated about every two scans, and this image can used until the next image was updated. Therefore, the sampling point for detecting cutting force by image process technique should be the point where the picture in SEM recorded video is updated, and the time resolution is about 0.20 s. Additionally, about every 900 frames, the time interval at which the video image is updated would become 0.19 s or 0.21 s, as shown in Fig. 5. This phenomenon may cause by the cumulative error and the electron beam blanking time. Therefore, based on the results of the SEM imaging mechanism, the frame where the image was updated in the SEM recorded video should be selected for the cutting force measurement. However, it should be noted that although the smaller the dwell time, the more measurement data can be obtained, it would also lead to the decrease of imaging SNR, which would lead to the decrease of measurement accuracy.

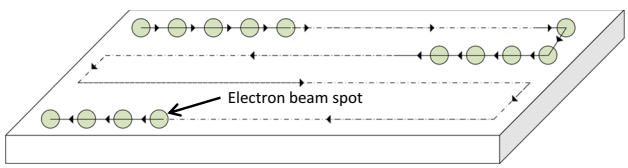

Fig. 4 SEM scanning trajectory

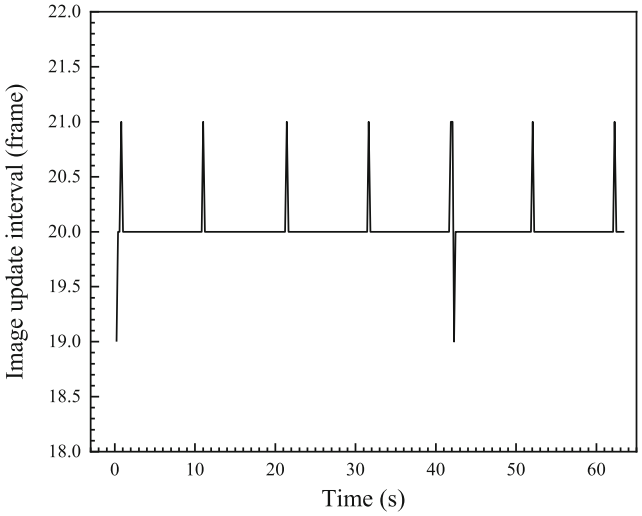

Fig. 5 The image update frames and its time interval

2.2.3 Detection of cutting tool movement status

In this study, the deflection change of the cutting tool is obtained by detection the trajectory of the cutting tool and then the cutting force was educed combined with tool shank stiffness calibration results. Therefore, the detection of the tool trajectory by image processing technology and the stiffness calibration of the tool shank are vital to the accuracy of cutting force measurement. Prior to nanocutting, platinum line was deposited on the cutting tool to provide a mark with contrast for cutting tool trajectory detection as shown in Fig. 6a. Then, cutting experiment and tool idle running experiment were conducted and the process was recorded by SEM. The video is divided into frames to extract the updated image in the video for cutting tool's position detection. Pretreatments (Guasfilter and Medfilter) were conducted to improve the SNR of the image. Then, OTSU method was used for threshold segmentation of areas interest with platinum line information shows in Fig. 6b. For the OTSU method is more applicable for such pictures that the object and background are single and different [37]. Then binarize the image based on the threshold calculated by OTSU method to extract the platinum line's information as shown in Fig. 6c. Subsequently, the platinum line's information was fitted to a vertical line as tool position information as shown in Fig. 6d. The position of the fitted line obeys the criterion of least square method, for it can minimize the sum of squares of errors of all the pixels of the platinum line's information. The position of cutting tool during idle running and cutting process was extracted by this method to calculate the deflection during nanometric cutting process by substrate the idle

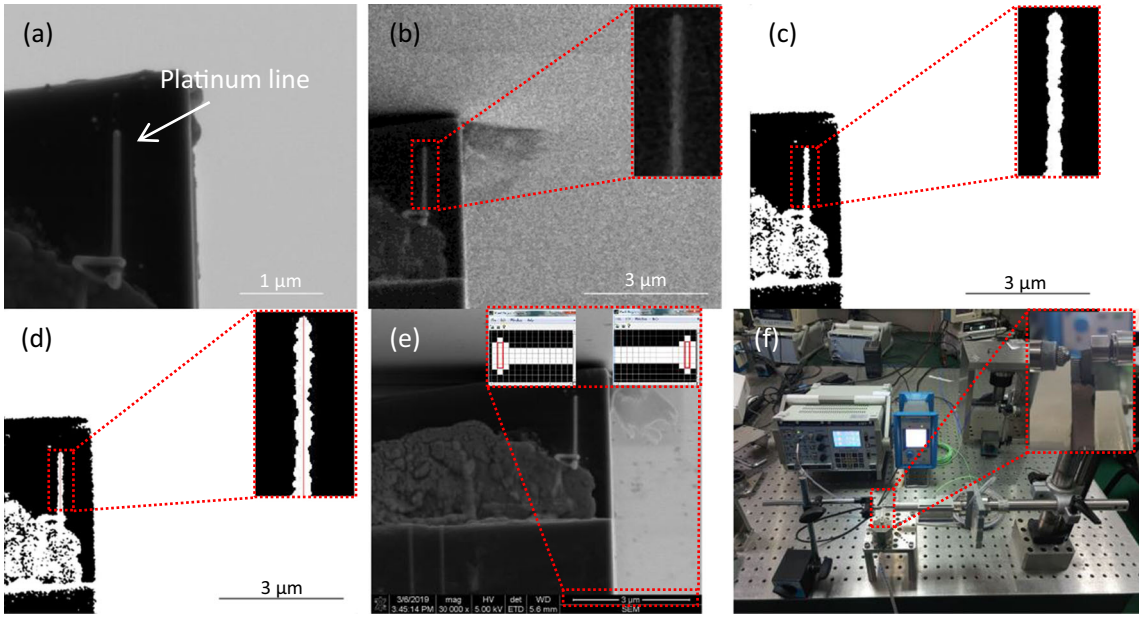

Fig. 6 The cutting force measurement method: (**a**) Deposit platinum line on diamond tool. (**b**) Areas interest with platinum line information. (**c**) Extraction of the platinum line's information. (**d**) Detection of Pt line position. (**e**) The length calibration for one pixel of SEM image. (**f**) Stiffness calibration of the tool shank

running position curve from cutting process position curve. Pixel calibration was performed, as shown in Fig. 6e, to transform the unit of deflection from pixel to nanometer. In this experiment, in order to obtain the entire cutting process with 7 μm travel range, the SEM magnification is set to be × 30,000. The scale of 3 μm under this magnification is composed of 361 pixels. The final pixel calibration result is about 8.31nm per pixel. At length, as Fig. 6f shows, the stiffness calibration experiment of the tool shank was conducted with a force sensor (Kistler Type 9207) and a displacement sensor (XSI 3000 LVDT) to educe the cutting force combined with the deflection measured by image processing technique. The force sensor was clamped and moved toward the tool shank by a displacement platform. The deflection of the tool shank was measured by the displacement sensor; the deflections information of the tool shank under different loading forces were recorded. The results of the tool shank stiffness calibration were listed in Table 1 and the average value K=ΔF/Δl=0.390 N/μm was used for the cutting force calculation. The standard uncertainty of this average stiffness calibration result is 0.012 N/μm, which is evaluated by Bessel formula:

Table 1 Tool shank stiffness calibration results

Number of measurements	1	2	3	4	5	6
ΔF (N)	0.70	0.79	1.35	1.45	2.17	2.29
ΔL (μm)	1.86	1.85	3.74	3.52	6.07	5.65
ΔF/ΔL (N/μm)	0.376	0.427	0.361	0.412	0.357	0.405

$$u\left(\overline{K}\right) = \frac{s(K)}{m} = \sqrt{\frac{\sum_{k=1}^{n}\left(K_k - \overline{K}\right)^2}{m(n-1)}} \quad (1)$$

Additionally, the resolution of the force sensor (FS) and displacement sensor (DS) will also lead uncertainty to the stiffness calibration results. The maximum relative uncertainty in the measurement range of this study is u_r(FS)=0.82% and u_r(DS)=0.31%, respectively.

2.3 Measurement methodology of the specific cutting energy

Specific cutting energy can be determined by taking the radio of cutting force to the area of cutting area, adopted from Huo and Cheng [38]. On the premise of neglecting the elastic recovery after nanocutting, the interaction area between the cutting tool and the sample in nanocutting can be roughly measured by detecting the cross-section formed after nanometric cutting. The morphology of the cutting grooves was characterized by atomic force microscope (AFM) with Bruker MultiMode8. Combined with the results of the cutting tool displacement during cutting process measured by image processing technology, the position of the cutting tool interact with the sample at corresponding time is determined. The information of the interaction section between the cutting tool and the sample at corresponding time is extracted as shown in Fig. 7. In this study, as shown in Fig. 1b, the cutting edge length of the tool used for 3C-SiC nanometric cutting experiment is at the micrometer

scale, while the cutting depth is at the nanometer scale. Therefore, the abscissa and ordinate of the cutting section after nanometric cutting of 3C-SiC adopt different scales in Fig. 7, which makes the cutting section shown in Fig. 7 is similar to the results of the nanoscratching results used nanoindentor. Actually, the morphology of the cutting section is a circular arc correspond with morphology of the flat nose diamond tool. Then, the area of interaction between the tool and the sample is calculated for the measurement of specific cutting energy. In nanometric cutting, material would be plowed outside of the groove and the plowed material is piled up alongside the groove [39]. This provides convenience for determining the boundary of cutting section area.

Figure 8 shows the cutting width (effective cutting edge length) and section area of machined surface with different cutting depths. As the cutting depth decrease in nanometer scale, the effective cutting edge length has a micrometer scale decrease. However, the cutting tool used in this experiment is a flat nose diamond tool sharped by FIB, whose nose radius is till non-negligible in nanometric cutting. A slight change in cutting depth will result in a change in the effective cutting edge length of the cutting tool. Correspondingly, the area of interaction between the cutting tool and the sample will increase non-linearly with the increase of cutting depth as shown in Fig. 6. It is foreseeable that this will greatly affect the specific cutting energy in nanometric cutting under different cutting depths.

3 Results and discussions

3.1 Morphology of the machined surface of 3C-SiC by online SEM observation

Figure 9 a–f show the nanometric cutting results of 3C-SiC for different cutting depths. The cutting depth was measured by AFM. When the cutting depth was less than 21 nm, smooth surface was obtained. As the cutting depth increased to 39 nm, Fig. 9c, d, pits and cracks appeared on the machined surface, which indicated that fractures happened in 3C-SiC nanometric cutting. As the cutting depth further increased, Fig. 9e, f, more typical forms of surface fractures occurred on the machined surface, indicating that the brittle regime gradually plays a major role [32].

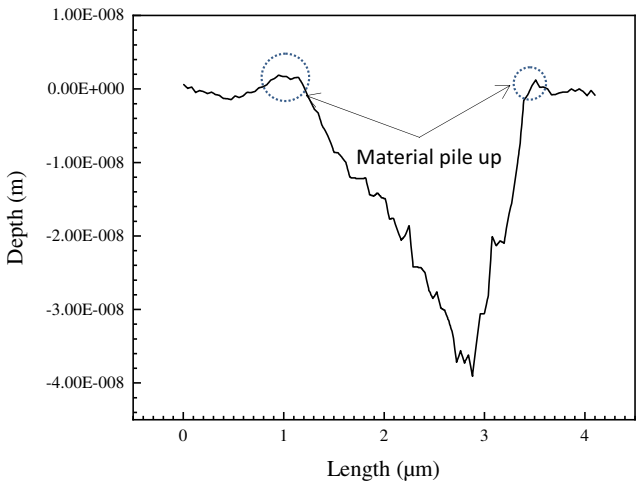

Fig. 7 The cutting section characterized by AFM

3.2 Cutting tool trajectory detection and the standard uncertainty of the detection method

3.2.1 The cutting tool trajectory detection results

The accuracy of cutting tool trajectory detection results is of vital importance for the accuracy of cutting force measurement and following analysis combined with specific cutting energy. The trajectory detection results were shown in Fig. 10. In order to reveal the difference in different material removal regime, the tool movement status during idle running process and nanometric cutting process with cutting depth 21 nm, 39 nm, and 48 nm were detected. It can be clearly seen that the tools have gone through the process from stationary to moving at a certain speed and then to the end of motion, indicated that the method can detect the change of the static and moving state of the cutting tool effectively. Additionally, the time between the beginning and the end of the cutting tool movement in idle running and nanometric cutting process were both 5965 frames (59.65 s). It proves that the nanometric precision motion stage has excellent motion reproducibility.

3.2.2 Uncertainty of the detection method

In order to verify the reliability of the image processing technology for extracting the position of the cutting tool and evaluate its uncertainty, the cutting tool was placed statically under the SEM observation and the process was recorded. The position of the cutting tool was detected and the result was shown in Fig. 11. The standard uncertainty of position detection of the cutting tool by image processing technology is 0.92 nm, which is evaluated by Bessel formula:

$$u(X_K) = s(X_K) = \sqrt{\frac{\sum_{k=1}^{n}\left(X_k - \overline{X}\right)^2}{n-1}} \tag{2}$$

The deflection of the tool shank during nanometric cutting is calculated by subtracting the position of the cutting tool during idle running from the position of the tool during nanometric cutting process. The standard uncertainty of the deflection measurement should be the synthesis of the standard uncertainty of two measurements. Its form is as follows:

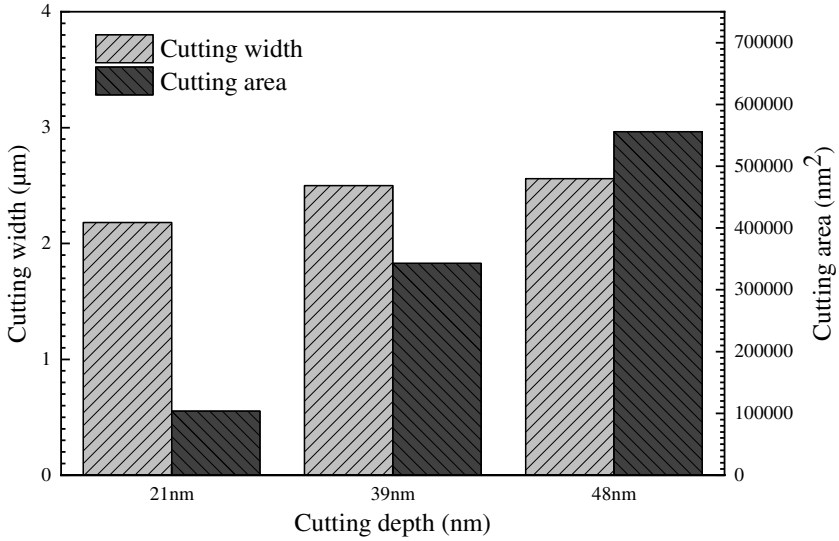

Fig. 8 Effective cutting edge length and section area of machined surface

$$u\left(X_{idle}-X_{cutting}\right)=\sqrt{u^2\left(X_{idle}\right)+u^2\left(X_{cutting}\right)} \quad (3)$$

The standard uncertainty of deflection detection is 1.30 nm.

3.3 Cutting force measurement and its standard uncertainty

3.3.1 Cutting force measurement results

Figure 12 shows the cutting force measurement results of 21 nm, 39 nm, and 48 nm cutting depth. The forces increase as the cutting depth is increased, as expected. Furthermore, not only the cutting forces are an important indicator for the assessment of local machining conditions, the magnitude and variation in the cutting forces is also found to be of use to distinguish ductile-regime cut from brittle regime cut in brittle materials [40]. The 21 nm cut appears mostly ductile, the 39 nm and 48 nm cutting depth represents the brittle regime gradually plays a major role. As the cutting depth increased, the force fluctuations are also increased, which suggests more of a brittle cut [34]. As other cutting parameters unchanged, the increase of cutting depth leads to the increasing number of atoms acted by the tool, which need to overcome more binding force obviously [41]. According to fracture mechanics [42], the fracture energy is equivalent to the surface energy newly generated by the mechanical machining in case of a perfectly brittle material. The newly created surface and corresponding number of broken atomic bonds by brittle fracture is larger than that in ductile mode. More energy should be consumed in creating the larger new surfaces and for breaking more atomic bonds suddenly, and this makes the cutting force

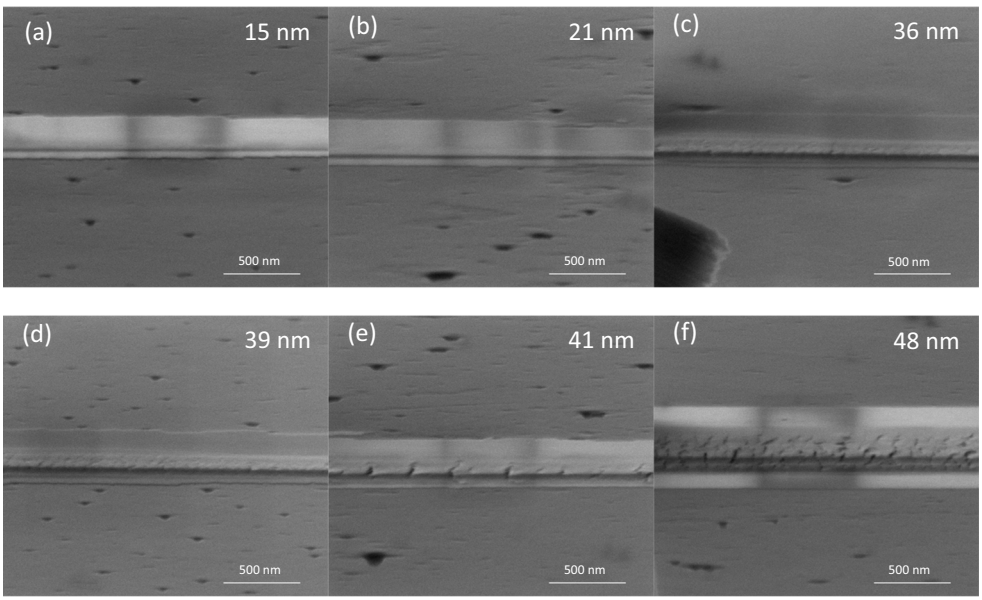

Fig. 9 SEM photographs of nanocutting surface morphology for different cutting depth (**a**) 15 nm, (**b**) 21 nm, (**c**) 36 nm, (**d**) 39 nm, (**e**) 41 nm, and (**f**) 48 nm

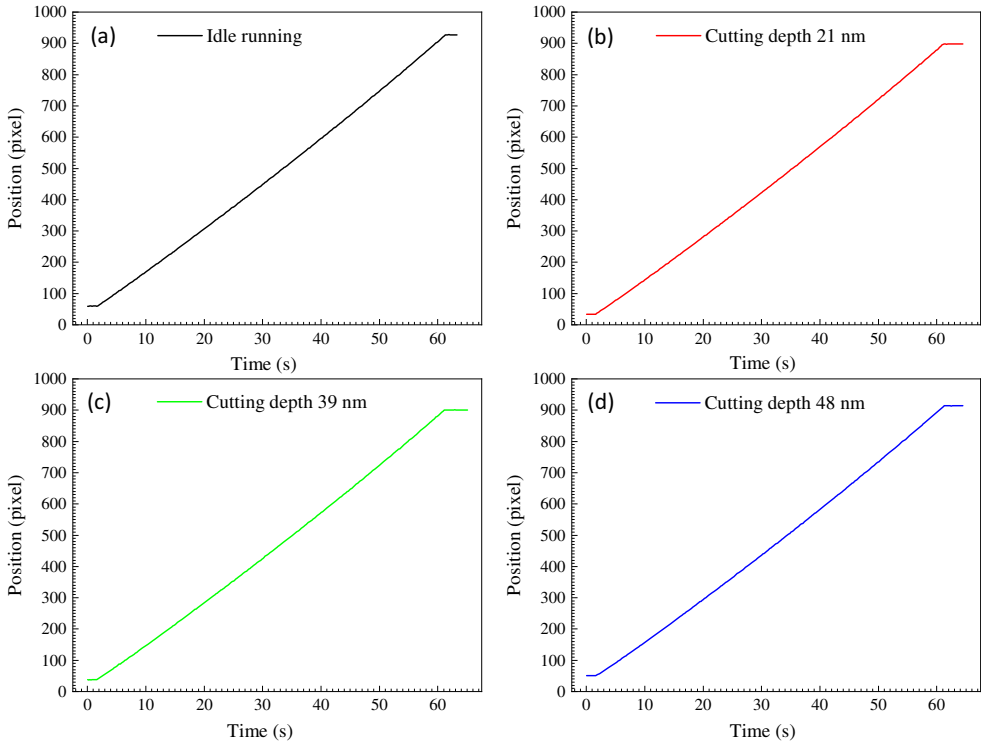

Fig. 10 Cutting tool trajectory detection results: (**a**) Idle running, (**b**) cutting depth 21 nm, (**c**) cutting depth 39 nm, and (**d**) cutting depth 48 nm

be dropped. In nanometric cutting, brittle fracture will produce pits with gradual thickness, which causes that after the pits are generated, the actual cutting depth will decrease and then gradually increase to the original cutting thickness. It means that the energy required for material removal should also gradually increase, which makes the cutting force accumulate and rise after falling. As shown in Fig. 9, the size and number of pits are larger with the cutting depth of 48 nm, corresponding to a longer time of energy accumulation after the formation of pits, and the fluctuation of cutting force is more severe. The size of the pits formed at 39 nm cutting depth is smaller than the 48 nm cutting depth, which means that the time of recovery to the original cutting depth is shorter after the pits are generated, and the energy required for material removal will be accumulated more quickly. The cutting force decreases suddenly and then rises rapidly, forming a sharp trough in the cutting force curve with 39 nm cutting depth. In the experiment of nanometric cutting brittle materials [43], the chips formed in nanocutting have both amorphous and polycrystalline components, but the latter accounted for a very small proportion of the whole. Although under SEM observation, nanocutting at 21 nm cutting depth is embodied as plastic removal, very few materials may have some brittle fracture events. When the cutting depth is 21 nm, the low cutting force may not be able to provide enough energy required for the brittle fracture event. The energy needs to be accumulated first, and then the energy release after the brittle fracture events corresponding to the reduction of cutting force. This may be the cause of the sharp peak in the cutting force curve at the cutting depth of 21 nm.

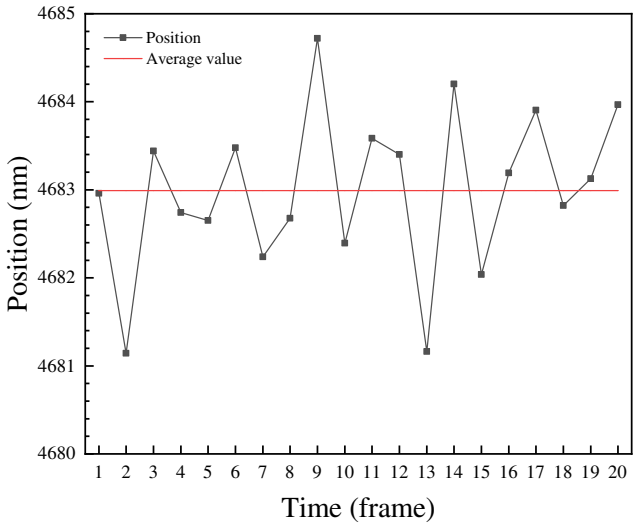

Fig. 11 Cutting tool position measured by the image processing method during the tool stationary period

3.3.2 Standard uncertainty of cutting force measurement

In this study, the cutting force was calculated by the cutting deflection detected with image processing technology and the stiffness calibration results of the tool shank. Its form is as follows:

$$F = \left(X_{idle} - X_{cutting}\right) \cdot K \tag{4}$$

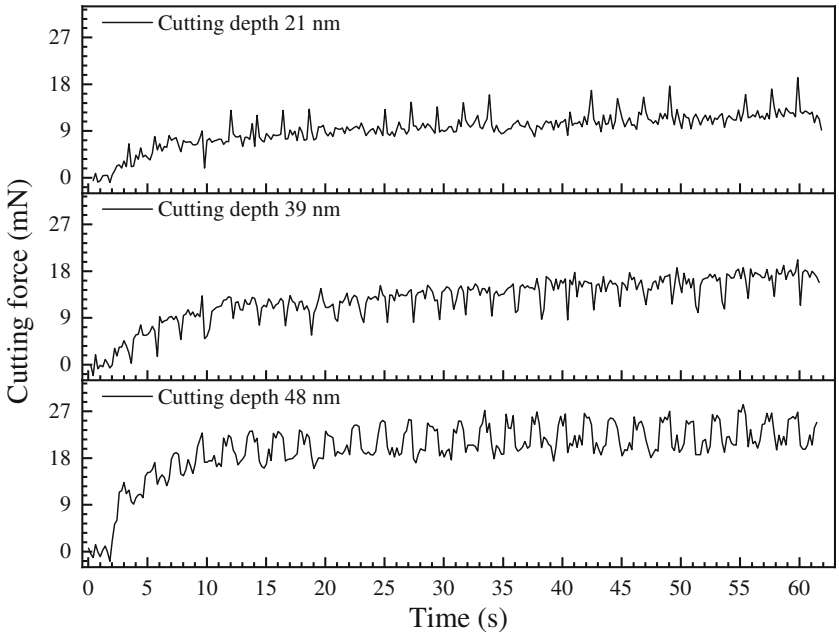

Fig. 12 The cutting force measurement results with cutting depth 21 nm, 39 nm, and 48 nm respectively

where X_{idle} is the movement status information of the tool idle running, $X_{cutting}$ is the movement status information of the tool during cutting process. K is the stiffness calibration results of the tool shank.

Table 2 summarizes the main sources of uncertainty contribution to the uncertainty of cutting force (F). The uncertainty caused by deflection detection using image processing technology and the stiffness calibration of the tool shank had been calculated in Section 2.2.3 and Section 3.2.2. According to the manufacturer of the nanocutting stage, the relative uncertainty of the repeat positioning accuracy $u_r(X_{repeat})$ is no more than 0.2% F.S..

The relative uncertainty of deflection detection by image processing technology was calculated using the average deflections under different cutting depths. The relative standard uncertainty of cutting force measurement under different cutting depths can thus be derived by the following equation:

$$u_r(F) = \sqrt{u_r^2\left(X_{idle}-X_{cutting}\right) + u_r^2\left(X_{repeat}\right) + u_r^2\left(\overline{K}\right) + u_r^2(FS) + u_r^2(DS)} \quad (5)$$

The uncertainty of the cutting force measurement under different cutting depths was shown in Table 3. The cutting force values used in the uncertainty calculation were the average cutting force under different cutting depths. The standard uncertainty in the current cutting force measurement method does not exceed 1 mN. The detection of the deflection by image processing technology is the main factor affecting the uncertainty of cutting force measurement.

3.4 Specific cutting energy measurement results

On the basis of the cutting force measurement, the specific cutting energy with cutting depths of 21 nm, 39 nm, and 48 nm were measured as shown in Fig. 13. In the cutting process where brittle removal regime gradually plays a major role (39 nm and 48 nm cutting depth), the specific cutting energy fluctuates in a relatively low range, approximately 31 GPa and 34 GPa. During the plastic dominated cutting process (21 nm cutting depth), the specific cutting energy is about 92 GPa, which is of good agreement with Noreyan's study [20]. The value in Noreyan's study was calculated as equal to the

Table 2 The sources of uncertainty in cutting force measurement

Sources of uncertainty	Symbol	Type	Relative uncertainty	Standard uncertainty
Deflection detection using image processing technology	$u(X_{idle}\text{-}X_{cutting})$	A	-	1.30 nm
Repeat positioning accuracy of nanocutting stage	$u(X_{repeat})$	B	0.2/-% F.S.	-
Resolution of force sensor	u(FS)	B	0.82%	5.77 mN
Resolution of displacement sensor	u(DS)	B	0.31%	5.77 nm
Stiffness calibration of tool shank	$u(K)$	A	3.03%	0.012 N/μm

Table 3 Uncertainty of cutting force measurement under different cutting depths

Cutting depth	21 nm	39 nm	48 nm
Average cutting force	9.76 mN	13.40 mN	20.74 mN
Relative uncertainty	6.09%	5.10%	4.03%
Standard uncertainty	0.59 mN	0.68 mN	0.84 mN

ratio of the average magnitude of the force applied in the scratching direction to the projected contact area.

Some researchers have pointed out that to generate a ductile cutting through purely applied stress (hydrostatic and shear) required that the pressures at the workpiece-chip interface be equal to, or higher than, the hardness of the material [44], which is taken to be around 37 GPa for 3C-SiC [45]. Patten et al. also found that the ductile removal of silicon nitride is caused by high-pressure phase transformation in the nanoindentation and grinding experiments, and the pressure is close to the hardness of the material [46]. Besides, similar phenomenon also appeared in 6H-SiC nanometric cutting [47]. In this study, with the cutting depth of 39 nm and 48 nm where the brittle removal regime gradually plays a major role, the pressure falls within the range expected to have brittle cutting of 3C-SiC, i.e., pressures less than 37 GPa. Under 39 nm and 48 nm cutting depth, the pressure is still partly higher than 37 GPa. This is because the 39 nm and 48 nm cut, while brittle cutting gradually dominates, but not pure brittle cutting, and there is also some plastic material removal. With the cutting depth of 21 nm, the non-negligible nose radius of the cutting tool leads the non-linear decrease of the cutting area. The specific cutting energy increases to more than 37 GPa (around 92 GPa), indicates that the material is removed being predominantly ductile. Similarly, the presence of high hydrostatic stress was found in nanometric cutting of 6H-SiC, which is about 88.2 GPa [48].

In this study, the morphology of the machined surface is used to calculate the cutting area. The error caused by elastic recovery and brittle pits is not taken into considered. This will cause the calculated cutting area to increase or decrease relative to the actual cutting area. However, it would not affect the tendency of the cutting area to decrease greatly due to the decrease of the cutting depth, leading to the increase of the specific cutting energy. That means high pressure would be applied to the material during nanometric cutting process under low cutting depth. Similar phenomenon that the non-linear increase of the specific cutting energy occurs with the cutting depth decrease where the tool edge radius becomes comparable to the cutting depth were also reported in other researches [49–51]. Further analysis combined with phase identification and dislocation will be explained in Section 3.5.

3.5 Phase identification and dislocation analysis

To detect the possible structural transformations in the nanometric cutting, EBSD characterizations with an accelerating voltage of 20 kV and a beam current of 2.4 nA were conducted across the machined and unmachined regions as shown in Fig. 14.

Significant differences can be observed from the phase identification and distribution for the machined and unmachined regions. In the machined regions, no backscatter Kikuchi patterns were found in almost all areas, indicating

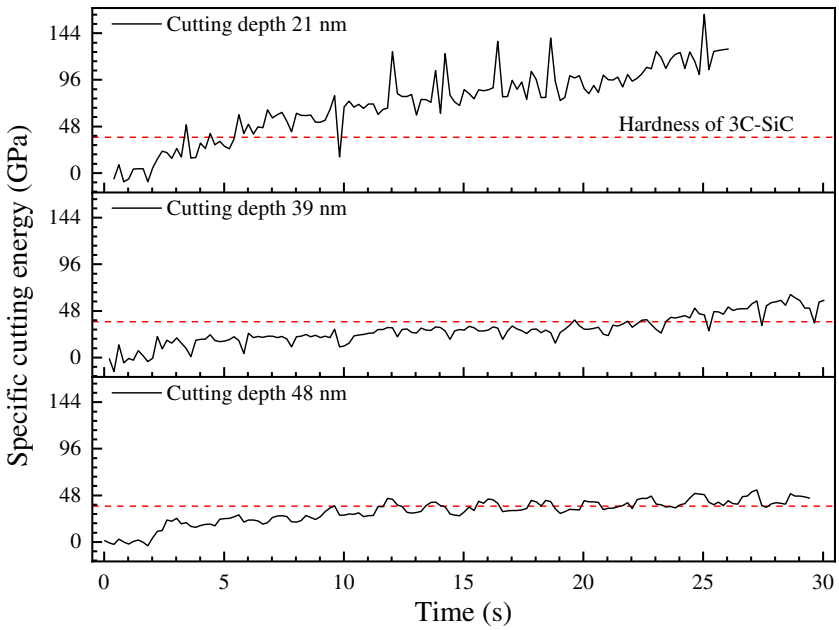

Fig. 13 Specific cutting energy with cutting depth 21 nm, 39 nm, and 48 nm respectively

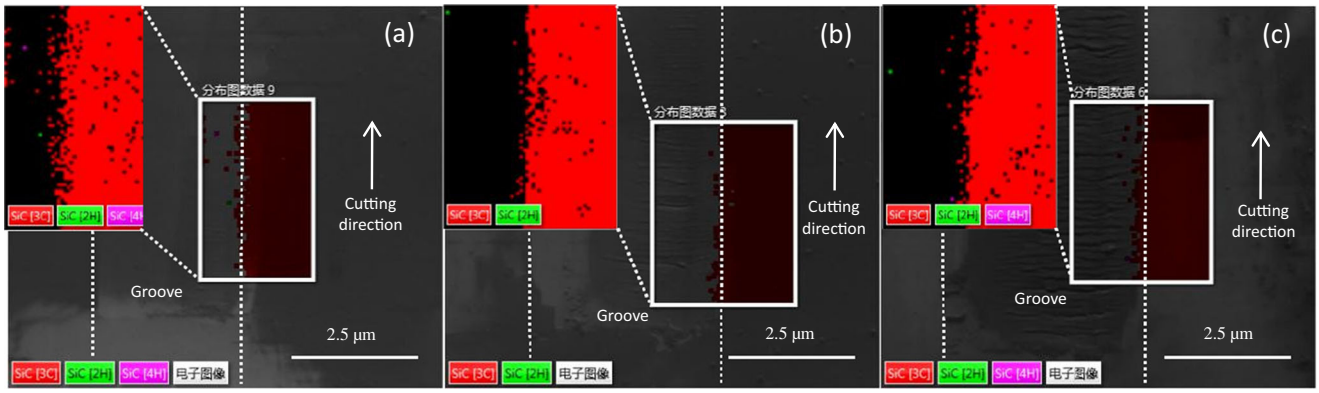

Fig. 14 EBSD results on phase identification with different cutting depth (**a**) 21 nm, (**b**) 39 nm, and (**c**) 48 nm

most of the machined materials are amorphous after nanometric cutting. In the regions alongside the cutting grooves, the material's EBSD pattern indexing rate is reduced compared with the EBSD result before nanocutting shown in Fig. 1c. It is speculated that a small amount of materials alongside the cutting grooves undergone amorphization due to the extrusion of the cutting tool [52]. Additionally, there is a very small amount of 2H and 4H phase transitions after nanometric cutting. Similar phase transition result also had been reported in 6H-SiC nanocutting [32].

In order to explore the degree of amorphization of materials and whether dislocation movements occur at different cutting depth, TEM samples were prepared at 21 nm, 39 nm, and 48 nm cutting depth as shown in Fig. 15. When the cutting depth is 21 nm, smooth surface was obtained with an amorphous layer about 13 nm. Under 39 nm cutting depth, the amorphous layer decreased to about 5 nm. When the cutting depth is 48 nm, the amorphous layer is substantially invisible, only amorphous region distributed inside the crystal region. Dislocations had not been found in the TEM sample. During the plastic dominated cutting process (21 nm depth of cut), the specific cutting energy fluctuates at about 92 GPa, which is much larger than that of brittle removal regime gradually plays a major role (39 nm and 48 nm depth of cut). The nanoscratching simulation study also shows that 3C-SiC will undergone amorphous under 89 GPa [20].

As the cutting depth decrease, the amorphous phase transformation of atoms in metamorphic layer aggravated. The occurrence of a high-pressure phase transformation of semiconductors and ceramics is often characterized by the amorphous remnant that exists, on the surface and within the chip, after processing. This amorphous remnant is a result of a back transformation from the high-pressure phase to an atmospheric pressure phase due to the rapid release of the pressure in the wake of the cutting tool. The high-pressure phase only exists while the pressure is applied. When the pressure is relieved, the material reverts to another phase [53]. In this study, a straight edge diamond tool sharped by FIB was used for nanometric cutting, but the nose radius is still non-negligible. As the cutting depth decrease, the cutting force and the cutting area both decrease, but the downward trend of the cutting area is more intense, which results in a larger specific cutting energy at a low cutting depth. Additionally, regardless of the nominal rake angle, either it is positive, negative, or 0°, the effective rake angle is always negative [52], which is known to increase the cutting and thrust forces due to the conditions of high hydrostatic pressure generated immediately underneath the cutting tool, which also promotes a ductile cut. It is believed that the plastic nature attributed to the ductile machining is a result of the material undergoing a high-pressure phase transformation to the metallic state in which the deformation occurs. It is believed that the high-pressure phase

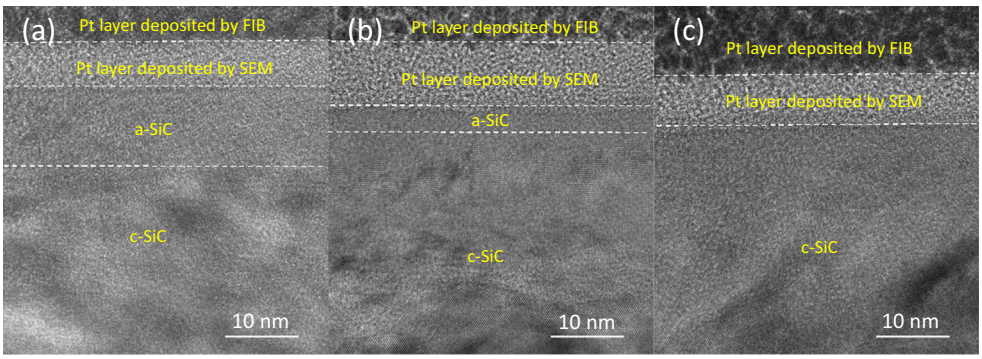

Fig. 15 TEM results with different cutting depth (**a**) 21 nm, (**b**) 39 nm, and (**c**) 48 nm

transform plays the major role in 3C-SiC ductile machining under the parameters of this experiment. In addition to considering the influence of the edge radius on HPPT, the influence of the nose radius should also be taken into consideration.

4 Conclusions

Based on the results from nanometric cutting on 3C-SiC, the conclusions can be drawn as follows:

1) The image processing technology is applied to the SEM imaging system. The imaging mechanism of the SEM is studied, and an image processing method suitable for the SEM imaging system was proposed. The feasibility of dynamic force measurement under high resolution observation based on SEM was verified.
2) Based on the limit space within the SEM vacuum chamber, a cutting force measurement method using image processing technology is proposed. The cutting force was educed by detecting the deflection of the cutting tool during the cutting process. The standard uncertainty in the current cutting force measurement method is less than 1 mN. This method provides a new way for the cutting force measurement of in situ SEM nanometric cutting devices.
3) AFM was used to extract the cross-section information of the cutting tool and the sample during the cutting process and the specific cutting energy at different cutting depth was calculated. The value fluctuates around 92 GPa in the cutting dominated by plastic removal regime, which is much larger than that of brittle removal regime gradually plays a major role. The size effect is the reason for the non-linear increase of cutting specific energy as the cutting depth decreases in the 3C-SiC nanometric cutting experiment.
4) As the cutting depth reduced to 21nm, a smooth machined surface is obtained, which means that ductile removal regime gradually plays a major role. The thickness of the amorphous layer and the specific cutting energy both increases. No dislocation movement was found in the TEM results, indicating that the HPPT plays the major role in 3C-SiC ductile machining under the parameters of this experiment.

Acknowledgements The study is supported by the National Natural Science Foundation of China (No. 51761135106, 51575389), the National Key Research and Development Program of China (2016YFB1102203), the State key laboratory of precision measuring technology and instruments (Pilt1705), the '111' project by the State Administration of Foreign Experts Affairs and the Ministry of Education of China (No. B07014), and the Harbin Core Tomorrow Science & Technology Co., Ltd.

Author contribution Zongwei Xu contributed to the conception of the study;

Zongwei Xu and Dongyu Tian performed the main part of the experiment;

Zongwei Xu, Junjie Zhang, Alexander Hartmaier, Bing Liu, and Lei Liu contributed significantly to analysis and manuscript preparation;

Zongwei Xu and Dongyu Tian performed the data analyses and wrote the manuscript;

Junjie Zhang, Alexander Hartmaier, Xichun Luo, Le Song, Lei Liu, and Zhanqi Zhou helped perform the analysis with constructive discussions;

Xuesen Zhao and Le Song helped perform part of the experiment.

Funding This study was funded by the National Natural Science Foundation of China (No. 51761135106, 51575389), the National Key Research and Development Program of China (2016YFB1102203), and the '111' project by the State Administration of Foreign Experts Affairs and the Ministry of Education of China (No. B07014).

Data availability All data and material information in this study are included in this published article.

Code availability The software application and custom code cannot be shared at this time as these also forms part of an ongoing study.

Declarations

Ethics approval and consent to participate Not applicable.

Consent for publication Not applicable.

Competing interests The authors declare that they have no known competing financial interests or personal relationships that could have appeared to influence the work reported in this paper.

References

1. Neudeck PG (2000) SiC technology. CRC Press Inc, Florida
2. Snead LL, Nozawa T, Ferraris M, Katoh Y, Shinavski R, Sawan M (2011) Silicon carbide composites as fusion power reactor structural materials. J Nucl Mater 417:330–339. https://doi.org/10.1016/j.jnucmat.2011.03.005
3. Yuan XL, Hobbs LW (2000) Influence of interatomic potentials in MD investigation of ordering in a-SiC. MRS Proc 650:R3.18.1–R3.18.6. https://doi.org/10.1557/proc-650-r3.18
4. Dzurak A (2011) Quantum computing: diamond and silicon converge. Nature 479:47–48. https://doi.org/10.1038/479047a
5. Fan HT, Xu CH, Wang ZH, Wang G, Liu CJ, Liang JK, Chen XL, Wei ZY (2014) Generation of broadband 17-μJ mid-infrared femtosecond pulses at 3.75 μm by silicon carbide crystal. Opt Lett 39:6249–6252. https://doi.org/10.1364/OL.39.006249
6. Shore P, Cunningham C, Debra D, Evans C, Hough J, Gilmozzi R, Kunzmann H, Morantz P, Tonnellier X (2010) Precision engineering for astronomy and gravity science. CIRP Ann Manuf Technol 59:694–716. https://doi.org/10.1016/j.cirp.2010.05.003
7. Loan PRV (1967) A study of polytypism in silicon carbide. Am Mineral 52:946–956

8. Singh D, Salem J, Kirihara S, Widjaja S (2013) Mechanical properties and performance of engineering ceramics and composites VIII. The American Ceramic Society, Florida
9. Mélinon P, Masenelli B, Tournus F, Perez A (2007) Playing with carbon and silicon at the nanoscale. Nat Mater 6:479–490. https://doi.org/10.1038/nmat1914
10. Fang FZ, Chen LJ (2000) Ultra-precision cutting for ZKN7 glass. CIRP Ann Manuf Technol 49:17–20. https://doi.org/10.1016/S0007-8506(07)62887-X
11. Fang FZ, Venkatesh VC (1998) Diamond cutting of silicon with nanometric finish. CIRP Ann Manuf Technol 47:45–49. https://doi.org/10.1016/S0007-8506(07)62782-6
12. He Y, Lai M, Fang FZ (2019) A numerical study on nanometric cutting mechanism of lutetium oxide single crystal. Appl Surf Sci 496:143715.1–143715.13. https://doi.org/10.1016/j.apsusc.2019.143715
13. Fang FZ, Zhang GX (2003) An experimental study of edge radius effect on cutting single crystal silicon. Int J Adv Manuf Technol 22:703–707. https://doi.org/10.1007/s00170-003-1593-2
14. Yoshida M, Onodera A, Ueno M, Takemura K, Shimomura O (1993) Pressure-induced phase transition in SiC. Phys Rev B Condens Matter 48:10587–10590. https://doi.org/10.1103/PhysRevB.48.10587
15. Shimojo F, Ebbsjo I, Kalia RK, Nakano A, Vashishta P (2000) Molecular dynamics simulation of structural transformation in silicon carbide under pressure. Phys Rev Lett 84:3338–3341. https://doi.org/10.1103/PhysRevLett.84.3338
16. Mishra M, Szlufarska I (2009) Possibility of high-pressure transformation during nanoindentation of SiC. Acta Mater 57:6156–6165. https://doi.org/10.1016/j.actamat.2009.08.041
17. Noreyan A, Amar JG, Marinescu I (2005) Molecular dynamics simulations of nanoindentation of β-SiC with diamond indenter. Mater Sci Eng B 117:235–240. https://doi.org/10.1016/j.mseb.2004.11.016
18. Zhao XF, Langford RM, Shapiro IP, Ping X (2011) Onset plastic deformation and cracking behavior of silicon carbide under contact load at room temperature. J Am Ceram Soc 94:3509–3514. https://doi.org/10.1111/j.1551-2916.2011.04674.x
19. Tang MJ (1995) Elastic instabilities and structural responses of β-SiC under stress. Dissertation, Massachusetts Institute of Technology
20. Noreyan A, Amar JG (2008) Molecular dynamics simulations of nanoscratching of 3C SiC. Wear 256:956–962. https://doi.org/10.1016/j.wear.2008.02.020
21. Goel S, Luo XC, Reuben RL, Rashid WB (2011) Atomistic aspects of ductile responses of cubic silicon carbide during nanometric cutting. Nanoscale Res Lett 6:589. https://doi.org/10.1186/1556-276X-6-589
22. Mishra M, Szlufarska I (2013) Dislocation controlled wear in single crystal silicon carbide. J Mater Sci 48:1593–1603. https://doi.org/10.1007/s10853-012-6916-y
23. Goel S, Stukowski A, Luo XC, Agrawal A, Reuben RL (2013) Anisotropy of single-crystal 3C–SiC during nanometric cutting. Model Simul Mater Sci Eng 21:2848–2855. https://doi.org/10.1088/0965-0393/21/6/065004
24. Wu ZH, Liu WD, Zhang LC (2017) Revealing the deformation mechanisms of 6H-silicon carbide under nano-cutting. Comput Mater Sci 137:282–288. https://doi.org/10.1016/j.commatsci.2017.05.048
25. Zhang JJ, Han L, Zhang JG, Liu HY, Yan YD, Sun T (2018) Brittle-to-ductile transition in elliptical vibration-assisted diamond cutting of reaction-bonded silicon carbide. J Manuf Process 45:670–681. https://doi.org/10.1016/j.jmapro.2019.08.005
26. Luo XC, Goel S, Reuben RL (2012) A quantitative assessment of nanometric machinability of major polytypes of single crystal silicon carbide. J Eur Ceram Soc 32:3423–3434. https://doi.org/10.1016/j.jeurceramsoc.2012.04.016
27. Chavoshi SZ, Luo XC (2016) Molecular dynamics simulation study of deformation mechanisms in 3C-SiC during nanometric cutting at elevated temperatures. Mater Sci Eng A 654:400–417. https://doi.org/10.1016/j.msea.2015.11.100
28. Liu L, Xu ZW, Tian DY, Hartmaier A, Luo XC, Zhang JJ, Nordlund K, Fang FZ (2019) MD simulation of stress-assisted nanometric cutting mechanism of 3C silicon carbide. Ind Lubr Tribol 71:686–691. https://doi.org/10.1108/ILT-03-2019-0096
29. Goel S, Luo XC, Reuben RL (2012) Molecular dynamics simulation model for the quantitative assessment of tool wear during single point diamond turning of cubic silicon carbide. Comput Mater Sci 51:402–408. https://doi.org/10.1016/j.commatsci.2011.07.052
30. Goel S (2012) Shear instability of nanocrystalline silicon carbide during nanometric cutting. Appl Phys Lett 100:535–538. https://doi.org/10.1063/1.4726036
31. Goel S, Luo XC, Reuben RL, Rashid WB, Sun JN (2012) Single point diamond turning of single crystal silicon carbide: molecular dynamic simulation study. Key Eng Mater 496:150–155. https://doi.org/10.4028/www.scientific.net/KEM.496.150
32. Xu ZW, Liu L, He ZD, Tian DY, Hartmaier A, Zhang JJ, Luo XC, Rommel M, Nordlund K, Zhang GX, Fang FZ (2020) Nanocutting mechanism of 6H-SiC investigated by scanning electron microscope online observation and stress-assisted and ion implant-assisted approaches. Int J Adv Manuf Technol 106:3869–3880. https://doi.org/10.1007/s00170-019-04886-6
33. Yan JW, Zhang ZY, Kuriyagawa T (2009) Mechanism for material removal in diamond turning of reaction-bonded silicon carbide. Int J Mach Tools Manuf 49:366–374. https://doi.org/10.1016/j.ijmachtools.2008.12.007
34. Patten J, Gao W, Yasuto K (2005) Ductile regime nanomachining of single-crystal silicon carbide. J Manuf Sci Eng 127:522–532. https://doi.org/10.1115/1.1949614
35. Fang FZ, Liu B, Xu ZW (2015) Nanometric cutting in a scanning electron microscope. Precis Eng 41:145–152. https://doi.org/10.1016/j.precisioneng.2015.01.009
36. Liu B, Fang FZ, Li R, Xu ZW, Liang YS (2018) Experimental study on size effect of tool edge and subsurface damage of single crystal silicon in nano-cutting. Int J Adv Manuf Technol 98:1093–1101. https://doi.org/10.1007/s00170-018-2310-5
37. Otsu N (2007) A threshold selection method from gray-level histograms. IEEE Trans Syst Man Cybern 9:62–66. https://doi.org/10.1109/TSMC.1979.4310076
38. Cheng K, Huo D (2013) Micro cutting mechanics. John Wiley & Sons Ltd., Manhattan
39. McGeough J (2001) Micromachining of engineering materials. Proc Inst Mech Eng B J Eng Manuf 216:607. https://doi.org/10.1243/0954405021520094
40. Goel S (2014) The current understanding on the diamond machining of silicon carbide. J Phys D Appl Phys 47:113–116. https://doi.org/10.1088/0022-3727/47/24/243001
41. Zhu Y, Xiang Z, Xie LL, Zhang YC, Zhao JC (2015) Study of the effects of cutting parameters on poly-silicon nano machining. Appl Mech Mater 697:369–372. https://doi.org/10.4028/www.scientific.net/AMM.697.369
42. Choi DH, Lee JR, Kang NR, Je TJ, Kim JY, Jeon EC (2017) Study on ductile mode machining of single-crystal silicon by mechanical machining. Int J Mach Tools Manuf 113:1–9. https://doi.org/10.1016/j.ijmachtools.2016.10.006
43. Fang FZ, Wu H, Zhou W, Hu XT (2007) A study on mechanism of nano-cutting single crystal silicon. J Mater Process Technol 184:407–410. https://doi.org/10.1016/j.jmatprotec.2006.12.007
44. Connor BPO, Marsh ER, Couey JA (2005) On the effect of crystallographic orientation on ductile material removal in silicon.

Precis Eng 29:124–132. https://doi.org/10.1016/j.precisioneng.2004.05.004
45. Tse JS, Klug DD, Gao F (2006) Hardness of nanocrystalline diamonds. Phys Rev B 73:140102(R). https://doi.org/10.1103/PhysRevB.73.140102
46. Patten JA, Fesperman R, Kumar S, McSpadden S, Qu J, Lance M, Nemanich R, Huening J (2003) High-pressure phase transformation of silicon nitride. Appl Phys Lett 83:4740–4742. https://doi.org/10.1063/1.1632031
47. Patten JA, Jacob J (2008) Comparison between numerical simulations and experiments for single point diamond turning of silicon carbide. J Manuf Process 10:28–33. https://doi.org/10.1016/j.jmapro.2008.08.001
48. Liu B, Xu ZW, Wang Y, Gao X, Kong RJ (2020) Effect of ion implantation on material removal mechanism of 6H-SiC in nano-cutting: a molecular dynamics study. Comput Mater Sci 174:109476. https://doi.org/10.1016/j.commatsci.2019.109476
49. Sawangsri W, Cheng K (2016) An innovative approach to cutting force modelling in diamond turning and its correlation analysis with tool wear. Proc Inst Mech Eng B J Eng Manuf 230:405–415. https://doi.org/10.1177/0954405414554020
50. Rahman MA, Rahman M, Mia M, Gupta MK, Sen B, Ahmed A (2020) Investigation of the specific cutting energy and its effect in shearing dominant precision micro cutting. J Mater Process Technol 283:116688. https://doi.org/10.1016/j.jmatprotec.2020.116688
51. Fang FZ, Xu FF (2018) Recent advances in micro/nano-cutting: effect of tool edge and material properties. Nanomanuf Metrol 1:4–31. https://doi.org/10.1007/s41871-018-0005-z
52. Fang FZ, Wu H, Liu YC (2005) Modelling and experimental investigation on nanometric cutting of monocrystalline silicon. Int J Mach Tools Manuf 45:1681–1686. https://doi.org/10.1016/j.ijmachtools.2005.03.010
53. Gogotsi YG, Kailer A, Nickel KG (1997) Phase transformations in materials studied by micro-Raman spectroscopy of indentations. Mater Res Innov 1:3–9. https://doi.org/10.1007/s100190050011